

Journal of Materials Chemistry C

Accepted Manuscript



This is an *Accepted Manuscript*, which has been through the Royal Society of Chemistry peer review process and has been accepted for publication.

Accepted Manuscripts are published online shortly after acceptance, before technical editing, formatting and proof reading. Using this free service, authors can make their results available to the community, in citable form, before we publish the edited article. We will replace this *Accepted Manuscript* with the edited and formatted *Advance Article* as soon as it is available.

You can find more information about *Accepted Manuscripts* in the [Information for Authors](#).

Please note that technical editing may introduce minor changes to the text and/or graphics, which may alter content. The journal's standard [Terms & Conditions](#) and the [Ethical guidelines](#) still apply. In no event shall the Royal Society of Chemistry be held responsible for any errors or omissions in this *Accepted Manuscript* or any consequences arising from the use of any information it contains.

ARTICLE

Role of oxygen plasma in the formation of oxygen defects in HfO_x films deposited at room temperature

Cite this: DOI: 10.1039/x0xx00000x

Received 00th January 2015,

Accepted 00th January 2015

DOI: 10.1039/x0xx00000x

www.rsc.org/

Mochamad Januar, Suhendro Purbo Prakoso, Sen-Yao Lan, Rama Krushna Mahanty, Shou-Yi Kuo, Kou-Chen Liu*

We investigate the oxygen-related defects induced in sputtered amorphous HfO_x thin films through oxygen plasma treatment. This study is devoted to the development of a room-temperature process to fabricate high-performance metal-insulator-metal (MIM) capacitors and thin-film transistors (TFTs) deposited on a glass/flexible substrate. Oxygen originated from the plasma can act as a source to control the surface composition of the HfO_x film. X-ray photoelectron spectroscopy analysis shows that different plasma powers stimulate different layers of stoichiometry within the films, which are represented by Hf 4f and O 1s core-level variations in terms of binding energy and peak broadening. The stoichiometry on the surface improves the quadratic voltage coefficient and frequency dispersion of the capacitances, whereas deepening the stoichiometry enhances the leakage current density, device uniformity and breakdown field strength. Recipes for the fabrication of both MIM and TFT devices through a simple-processed plasma treatment at low temperatures are provided. Herein, we demonstrate HfO_x-based devices encompassing a MIM capacitor with low-frequency dispersion and a voltage nonlinearity of 12 ppm/V² as well as an a-IGZO TFT with a mobility of 21 cm²/V-s, a threshold voltage of 2.66 V, an I_{on}/I_{off} ratio of 1.09 × 10⁷ and a subthreshold swing of 0.258 V/dec.

Introduction

Deploying hafnium oxide (HfO₂) high-κ dielectrics in metal-insulator-metal (MIM) capacitors and thin-film transistors (TFTs) is essential for the fabrication of low-cost transparent and/or flexible electronic devices due to their large permittivity, low leakage current and high breakdown strength.^{1–3} In a capacitor, this high-κ maintains a capacitance density of above 5 fF/μm² and a leakage current density below 10⁻⁸ A/cm² while keeping the quadratic voltage nonlinearity coefficient below 100 ppm/V².² Subsequently, this material enables the full room-temperature fabrication of transparent amorphous metal-oxide TFTs for the active matrix in display applications, such as amorphous indium-gallium-zinc-oxide (a-IGZO)-based TFTs.³ With this oxide technology, devices that possess high mobility and high switching speed capability with a large area of uniformity and smoother interface due to the absence of grain boundaries could be realized.³ Their low-temperature feature allows them to be manufactured on inexpensive substrates, such as glass, flexible plastic and paper.^{4,5}

For large-scale industrial applications, magnetron sputtering facilitates the production of low-temperature HfO₂ films with a large area of uniformity at a relatively high growth rate.¹ This

technique offers lower contamination with a compositional consistency between the sputter target and deposited film.^{6,7} Nevertheless, similar to other known low-temperature deposition techniques, such as atomic layer deposition and the solution process,^{3,8} the as-deposited HfO₂ films from the sputtering process generally have nonstoichiometric compositions with either excessive or deficient oxygen concentrations (HfO_x).^{8–11} To realize HfO_x on actual devices, an exact stoichiometric composition is required to avoid traps that can lead to poor device performance.^{12,13} For this reason, high-temperature annealing is frequently performed after deposition to improve the stoichiometry.^{9,11} In elevated temperature processing, the defects are likely to be highly active, and thus, the incoming oxygen sources will easily diffuse into the vacant sites to minimize the total energy of the system.¹⁴ However, this process is generally followed by rapid crystallization that encourages the emergence of grain boundaries.^{11,15,16} The oxygen vacancies from the oxygen deficiency sites may induce interface states at the grain boundaries, which are responsible for Fermi-level pinning effects and a diffusion path for electron tunneling or mobile ions, enabling a higher current leakage.^{11,15,17} Moreover, the addition of the thermal budget

breaks the room-temperature corridor, which may damage the aforementioned transparent glass/flexible substrate.¹⁸

On the other hand, oxygen plasma treatments can be developed to suppress these oxygen-related defects at room temperature. It was recently reported that this plasma exposure can improve the leakage current and the dielectric breakdown performance of HfO_x films prepared through sputtering without any thermal annealing.¹⁹ This oxygen treatment was also reported to lower the post-annealing temperature necessary to achieve stoichiometric HfO_2 .^{3,18} Unfortunately, a clear understanding of how the oxygen plasma treatment organizes the stoichiometry, including its role in improving the dielectric performance, is still lacking. Consequently, the realization of a fully room-temperature procedure for preparing high-quality HfO_x thin films has been hindered.

In this work, HfO_x thin films were prepared by sputtering followed by oxygen plasma treatment at room temperature without thermal annealing. The role of stoichiometry was investigated by varying the oxygen provided to the film through different plasma powers. This variant oxygen supply is expected to produce differences in chemical compositions and Hf-related bonding so that samples with distinct stoichiometries can be produced. Once oxygen ions diffuse into the films to initiate the stoichiometric formation, a charge transfer and relaxation mechanism must follow due to their ionicity.^{14,20} This process is expected to shift the Hf-O bond strength and drive a change in their chemical states. By monitoring these chemical trends and the electrical device characteristics, one can obtain more information about how chemistry controls the dielectric performances, such as the change in voltage nonlinearity, leakage current, breakdown field, and device uniformity. In this paper, descriptions of the chemical changes induced by the plasma treatment are discussed in detail via X-ray photoelectron spectroscopy (XPS) analysis.

Experimental Section

We investigated the characteristics of HfO_x insulator films by fabricating MIM capacitors and an n-type IGZO TFT on ITO-coated glass substrates with a sheet resistance of $4.3 \Omega/\square$. The ITO substrates were ultrasonically cleaned using DI water, acetone and an isopropyl alcohol solution, followed by a 200 W oxygen plasma treatment under a working pressure of 20 mTorr, an oxygen flow of 2 sccm and a treatment time of 4 min. This treatment is important to reduce surface contamination and roughness to suppress the leakage current.^{3,21} Approximately 80 nm of HfO_x dielectric film was deposited by DC reactive magnetron sputtering using a 3 inch diameter Hf metal target at room temperature. The sputtering process was conducted with a working pressure of 5 mTorr and a DC power of 150 W under an atmosphere of 5% O_2 and 95% Ar. The as-deposited HfO_x samples were then subjected to reactive oxygen plasma treatment with different RF powers of 100, 200 and 300 W for 4 min under working pressure of 20 mTorr and oxygen flow of 2 sccm. For brevity, these different samples will be denoted as S0, S100, S200, and S300,

respectively. The plasma treatments were performed in a capacitive reactive-ion etching tool with the substrate electrode was connected to a 13.56 MHz RF-generator (Huttering PFG 300 RF), and the upper electrode was grounded. The influences of these different plasma conditions on the chemical compositions of the films were examined by XPS using a PHI 5000 VersaProbe (ULVAC-PHI, Chigasaki, Japan) system with a micro-focused (100 μm , 21.4 W) Al X-ray beam. During the measurement, *in situ* argon sputtered cleaning was used to clean the surface contamination and then varied over time to investigate the chemistries beneath the surface. Further material characterizations, such as X-ray diffraction (XRD) and transmission electron microscopy (TEM), were also performed to determine the amorphousness of the HfO_x samples. A 100 nm Al layer was then coated using thermal evaporation with shadow mask patterning techniques for the top electrodes of the Al/ HfO_x /ITO capacitor structure. For the TFT fabrication, n-channel a-IGZO was sputtered on top of the HfO_x prior to the source/drain thermal Al deposition. It was also patterned by shadow masks. Finally, I-V and C-V characteristics were measured by Agilent E5270B and Agilent E4980A parameter analyzers.

Results and discussion

The structures of HfO_x thin films prepared on glass and ITO/glass substrates were investigated by XRD measurement. As shown in Figure 1, peaks can be observed in the samples deposited on the ITO/glass substrate, but they primarily come from the body-centered cubic (bcc) structure of the polycrystalline ITO.²² Although a residual peak of monoclinic (m) HfO_2 appeared at 34° (002 orientation), its intensity is less than 15% of that of the (222) ITO and is reduced by increasing the plasma power. Additionally, the (-111) and (111) m- HfO_2 orientations have been reported to be more favorably grown on ITO than the (002) or (200) planes.²³ Moreover, no significant peak appears in the samples deposited on the bare glass. These

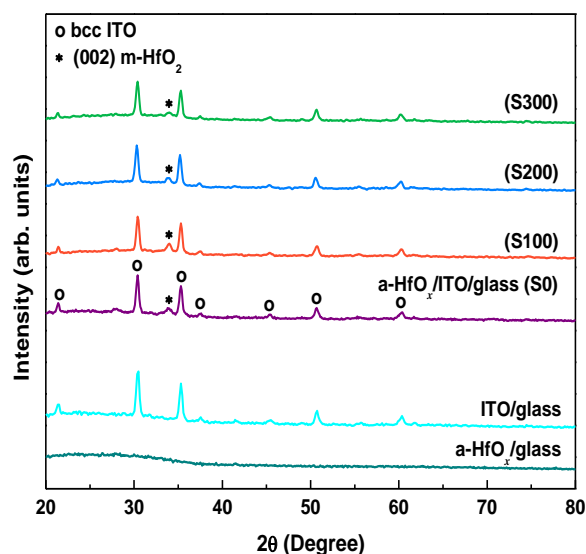


Figure 1. X-ray diffraction analysis to confirm the amorphousness of the HfO_x films.

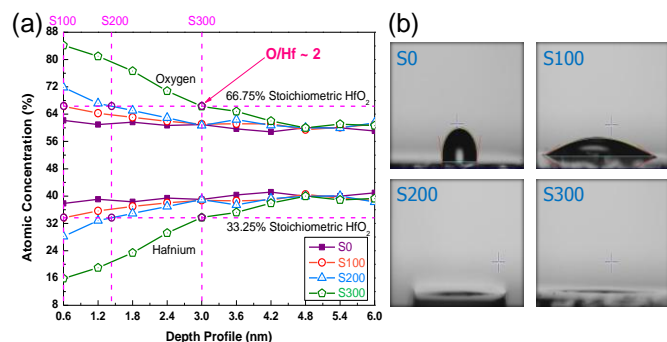


Figure 2. (a) Atomic concentrations of Hf and O elements against the depth profile and (b) contact angle analysis, for different RF powers of the oxygen plasma treatment.

lines of evidence suggest that the peak of $m\text{-HfO}_2$ is not intense enough to confirm a crystallization, so that its existence could be neglected.²⁴ Thus, the resulting HfO_x films are verified to be amorphous. This is further confirmed by the cross-sectional TEM image in Figure 12(a). The absence of nanocrystallites in the image demonstrates that the amorphous nature of the $a\text{-HfO}_x$ layer is preserved even after implementation in a TFT device.

Figure 2(a) shows oxygen concentrations in $a\text{-HfO}_x$ samples in respect to equivalent depth profiles (with a step of 0.6 nm) for different powers of plasma treatment. As the oxygen content of the non-treated sample (S0) at a 0.6 nm depth level is similar to that in the bulk region, the XPS analysis was started from this surface level for all samples. This approach is important to avoid ambient surface contaminant interference to the analysis. Furthermore, Figure 3 shows that the spectra of Hf 4f and O 1s core-levels in S0 are unchanged with the depth increases, verifying that the Ar sputtering during XPS depth profiling does not modify the O/Hf states. Thus, chemical changes on the samples can be derived solely from the plasma treatment. In S0, the percentage of O/Hf atomic ratio is below the HfO_2 stoichiometric value for all depth profiles (x is about 1.42-1.65), revealing the oxygen deficiency of the as-deposited sample. By imposing the oxygen plasma treatment, the oxygen ratio is progressively intensified on the surface with the power increases. A proper stoichiometric O/Hf ratio ($x \approx 2$) occurs at 0.6 nm in S100, at approximately 1.2 nm in S200 and at 3.0 nm in S300. This indicates that the oxygen permeates through the bulk to a depth of 3.0 nm upon increasing the RF power to 300 W. Furthermore, the contact angle analysis demonstrates a similar tendency from the improvement of the HfO_x surface hydrophilicity. As shown in Figure 2(b), increasing the power makes the contact angle between the surface material and H_2O droplet smoother. This effect occurs because a greater concentration of oxygen on the HfO_x surface attracts the droplets of water molecules more strongly, spreading them over the surface and resulting in a lower contact angle.

The chemical states of the $a\text{-HfO}_x$ samples can be examined through the center positions of the XPS spectra in terms of binding energy (BE). The BEs of all measured signals were calibrated by setting the C 1s peak for adventitious carbon at 285 eV to account for sample charging.^{19,25} The spectra were

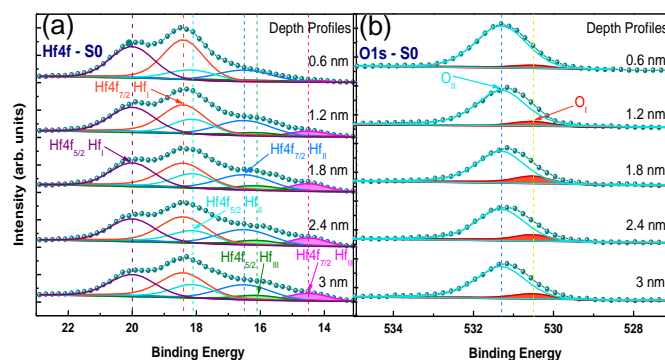


Figure 3. (a) Hf 4f and (b) O 1s core-level spectra of XPS measurements for the non-treated sample.

then carefully deconvoluted using the Gaussian-Lorentzian distribution function, which included prior Shirley background subtraction. Figure 3(a) shows the Hf 4f core-level of the non-treated sample. In this sample, the spectra appear as broad shoulders, which indicate that the signals may consist of different BEs of Hf 4f species. This appearance is reasonable to be formed considering the as-deposited HfO_x samples are amorphous and having a less oxygen content ($x < 2$),²⁶ as confirmed by the XRD and O/Hf ratio. Correspondingly, the Hf 4f spectra could be fitted to the entire region by adding some additional peaks, at 16.5 & 18.1 eV (Hf_{II}) and 14.5 & 16.1 eV (Hf_{III}), next to the main peaks (Hf_{I}) that located at 18.4 & 20.0 eV. The two BEs of each state correspond to the Hf 4f_{7/2} and Hf 4f_{5/2} doublet spin-orbit splitting, respectively. The relative areas of these doublet signals follow the theoretical ratio of 4:3 with different BEs maintained constantly at 1.6 eV and the full widths at half-maximum (FWHM) of all fitting curves below or equal to 2 eV, to constrain the fingerprint of each species.²⁷ According to the relative area calculations (Figure 4a), the percentages of the Hf_{I} , Hf_{II} and Hf_{III} signals are 55.4%, 34.0% and 12.6%, respectively, in the bulk. This ratio represents highly disordered Hf-O bonds in which the Hf atoms contribute to more diverse bonding configuration, so that various types of $\text{Hf}^{x+}\text{-O}$ species coexist in the sample. Both the Hf_{II} and Hf_{III} features can be straightforwardly identified as the $\text{Hf}^{2+}\text{-O}$ suboxide and Hf-metal bonding states, respectively.²⁷⁻³⁰ However, the Hf_{I} 4f_{7/2} main peak lies at 1 eV away from the stoichiometric BE ranges (16.7-17.4 eV),^{25,31-35} which is unlikely to be interpreted as a typical $\text{Hf}^{4+}\text{-O}$ bonding state. The occurrence of such higher BE may be caused by the abundant presence of oxygen defects that disturb the neighboring Hf atoms.^{36,37} The Hf-O bonds are possibly modified as they are formed between atoms with nontrivial coordination numbers.²⁶ This condition leads to bond length changes and BE shifting to a higher energy.^{33,36}

The nonstoichiometric tendencies of the as-deposited film are supported by the O 1s counterpart in Figure 3(b). The data counts of the oxygen spectra can be consistently deconvoluted by two constant peak positions centered on 530.5 (O_{I}) and 531.3 (O_{II}) eV. The lowest peak is attributed to the formation of fully oxidized oxygen states,^{26,28,38-41} which is minor in S0 (only 10.8%). On the other hand, the O_{II} shoulder dominates the

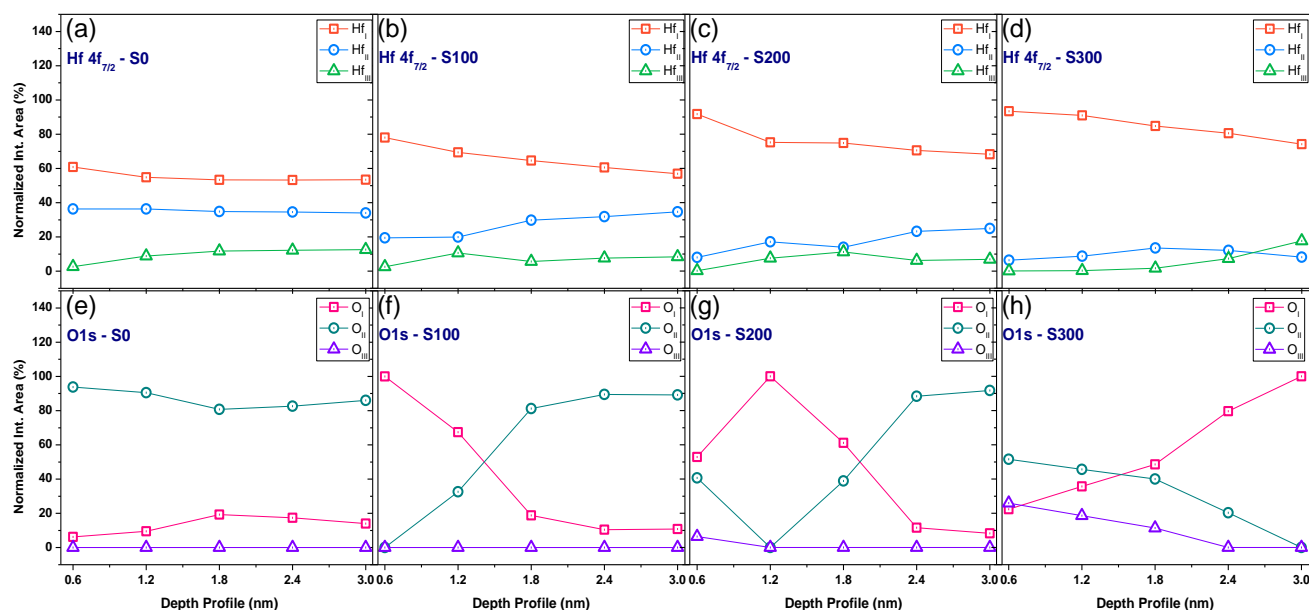


Figure 4. Relative area of the deconvoluted peaks in the Hf 4f and O 1s core-level spectra.

oxygen states by covering 89.2% of the total area. This domination signifies the nonstoichiometric properties of the film, which is in line with the Hf 4f result. However, judging from the broader spectra on the Hf 4f side, the single peak of O_{II} could not be correlated to only one single species of the Hf-related bonding. Instead, the O_{II} should be corresponded to the collective contributions of all nontrivial oxygen formations that may occur.²⁶ In S0, the highly presence of O_{II} component quantifies the large numbers of oxygen defect states that exist in the vicinity of the Hf-O bonds with nontrivial formations,^{26,28,38–41} e.g., nontrivial coordination and/or nontrivial bond length. This interpretation is in consistent with the broader Hf 4f spectra and the oxygen deficiencies that were displayed in the O/Hf atomic ratio.

Both the Hf 4f and O 1s photoelectron trends indicate that the Hf-O lattices are surrounded by extremely large oxygen deficiencies or Hf-metal rich environments that possibly drive

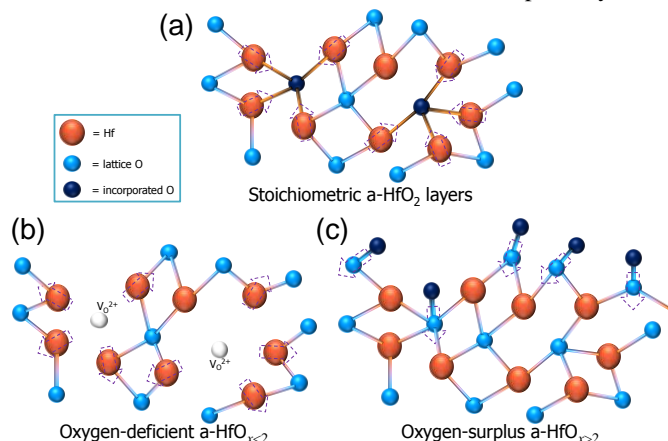


Figure 5. Illustrated structures for (a) a fully oxidized stoichiometric HfO_2 lattice sites, (b) the oxygen deficient HfO_x in which some oxygen vacancies ($\text{V}_{\text{O}^{2+}}$) are induced and (c) the oxygen rich HfO_x in which some O-O bonds are formed. For simplicity, the stoichiometric state is illustrated by the three-fold of Hf and four-fold of O coordinations.

the BE shifting in the neighboring Hf atoms.^{36,37} The mechanism is illustrated in Figure 5. Cho *et al.* experimentally confirmed that due to their ionicity, these defects may induce lattice relaxation and bond length changes at the Hf-O bonding sites.³³ Once an oxygen atom disappears from its original position in a stoichiometric state (Figure 5(a)), a doubly ionized positive oxygen vacancy ($\text{V}_{\text{O}^{2+}}$) is more favorable to be formed, and hence, the equilibrium positions of the nearest Hf atoms are disturbed.^{20,33} These Hf atoms tend to relax outward and attempt to re-establish bonding with their nearest oxygen neighbors, constructing a new stable equilibrium position, as illustrated in Figure 5(b). In such circumstance, the mean distance of the Hf-O bond is relatively reduced compared to the earlier position, and therefore, a larger BE is observed.^{20,33,36} Thus, the broader Hf 4f spectra along with its higher BE elucidates the nonstoichiometric properties of the as-deposited amorphous HfO_x films that are commonly yielded from a low-temperature deposition.^{8,9}

Figure 6 shows the spectra of HfO_x film with 100 W power of plasma treatment (S100). Comparing with Figure 3, the spectra of bulk states of S100 at depths lower than 1.8 nm are identical to the non-treated sample, which implies that the

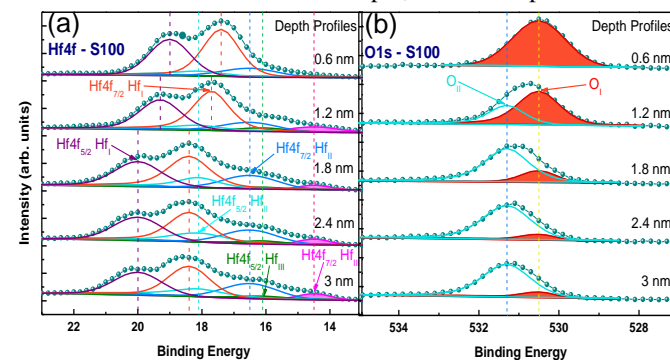


Figure 6. (a) Hf 4f and (b) O 1s core-level spectra of XPS measurements for 100 RF power of plasma treatment.

oxygen plasma treatment only controls the chemistries around the films surface. In the affected region, the center of the Hf $4f_{7/2}$ signal gradually shifts from 18.4 to 17.7 eV and eventually reaches 17.4 eV (at 0.6 nm), which is in agreement with the reported stoichiometric BE for a thick HfO_2 .^{31,35} If this peak shifting explains Hf-O stoichiometric oxidation mechanism, the other components are either the Hf 4f or O 1s BEs, and their shoulder areas are expected to follow the same trend.¹² Through the shifting, the broadening of the Hf 4f spectrum is reduced. As detailed in Figure 4(b), the relative area of the Hf_I species increases from 55.4% to 77.9%, and Hf_{II} and Hf_{III} decrease from 34.0% to 19.5% and 12.6% to 2.6%, respectively. Apparently, this peak sharpening (at 17.4 eV) implies the enhancement of Hf-O stoichiometric formation, which reveals the autograph of the oxygen plasma in passivating the oxygen vacancies. This hypothesis is well corroborated by the fully enhanced O_I peak center on the O 1s side (Figure 6(b)). The O_I species approaches 100%, whereas its O_{II} counterpart decreases from 89.2% to zero at the 0.6 nm depth level. This alteration quantifies the number of fully oxidized oxygen atoms fastened to the surrounding Hf atoms, exhibiting the formation of a stoichiometric HfO_2 layer with Hf^{4+} and O^{2-} valences.^{12,38} This result agrees with Figure 2 in which the O/Hf atomic ratio of S100 displays an appropriate stoichiometric composition of $x \approx 2$ at a depth of 0.6 nm. Therefore, the Hf_I $4f_{7/2}$ peak at 17.4 eV corresponds to the O_I peak, describing the fully oxidized stoichiometric layer formation in the sample.

By increasing the plasma powers to 300 W, the oxygen concentration generally increases from 60% to 84% on the surface of the samples (see Figure 2(a)). Nevertheless, this excess oxygen does not all correspond to the stoichiometric configuration. Although an identical stoichiometric layer is found shifting to a deeper level at around 1.2 and 3 nm for S200 and S300, respectively, the upper layer retains much richer oxygen content. In the rich region, the O 1s spectra broaden towards the higher BEs, as depicted in Figure 7(b) and (d). Consequently, the O_{II} species reappears, and a new higher BE oxygen species (O_{III}) was introduced at 532.15 eV to maintain the FWHM of the O_{II} fitting ≤ 2 eV. In S200, the O_{II} relative area initially decreases from 91.7% (3 nm) to 0.1% (1.2 nm) followed by the Hf_I BE shift from 18.6 (3 nm) to 17.4 (1.2 nm) eV, which occurs due to the aforementioned enhancement of the stoichiometric formation. However, the O_{II} species

increases to 40.6% at 0.6 nm, and a 6.5% O_{III} shoulder is subsequently created. This O_{II} reaches 51.6% at 0.6 nm in S300, and the O_{III} species reaches 25.9%. The trend is correspondingly followed by the reduction of the stoichiometric species (O_I), which declines to 52.9% and 22.5% at the surfaces of S200 and S300, respectively. Moreover, the nonstoichiometric sign is also engraved on the Hf 4f side via shifting to the higher BE (Figure 7(a) and (c)).

To enlighten the explanation, the Hf $4f_{7/2}$ peak positions to the oxygen changes are summarized in Figure 8. From the figure, the BE shifts of the metal core-level peaks decrease continually with increasing oxygen composition until the stoichiometry reaches, and slightly increase as the oxygen further increases. In Hf-rich region, the higher Hf 4f BEs including its broadening spectra, are more likely due to variation in coordination environments because of the largely presence of the metallic Hf-components, *i.e.*, the Hf-O bonds are strongly modified because of the largely presence of V_O^{2+} . However, this effect would not be expected for the O-rich environment, because most of the Hf atoms on the surface have probably been oxidized with a fully coordinated oxide. This can be seen from the disappearances of the Hf^{2+} -O and Hf-metal species on the Hf 4f signal in S300. Further distinguishes also can be seen from the induced Hf 4f shifts that are not more than 0.4 eV even as the oxygen content exceeds 75% of the O/Hf atomic ratio ($x > 3$).

In fully oxidized condition, the excess oxygen are hardly to gain electron from lattice Hf atoms, so that they might present only in the form of atomic interstitials.⁴² The recent theoretical first principle studies have demonstrated that the interstitial oxygen form a dumbbell type configuration with lattice oxygen in Hafnia and Zirconia, forming Hf-O-O-Hf configuration with O-O covalently bonded.^{20,43} To accommodate the interstitials, the lattice oxygen strongly relaxes from its original position. However, in contrast to the presence of V_O^{2+} , the relaxation on the nearest Hf atoms to the pair is quite small (≈ 0.05 Å),⁴³ and thus, leading to only small Hf 4f BE shifting in the present of large amount of the interstitials. Furthermore, a similar small shifting on the Hf 4f peak was also reported to occur due to a change in ionic environment as some of the second adjacent Hf atoms were substituted by more electronegative atoms.^{44,45} Owing to high electronegativity of the incorporated oxygen, the small Hf 4f shift can also be explained by this mechanism.

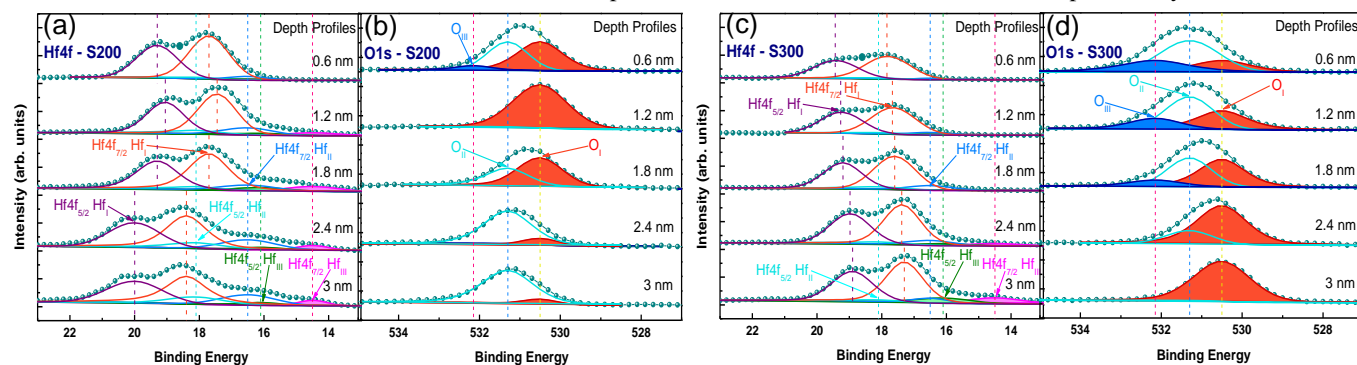


Figure 7. Core-level spectra of Hf 4f and O 1s for S200 and S300.

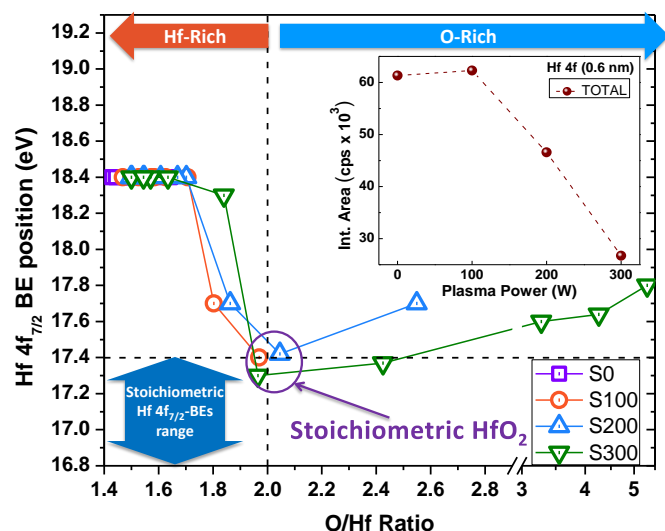


Figure 8. Hf 4f_{7/2} binding energy position with respect to a wide range of oxygen content, which deduced from the depth profiles of each sample. Additionally, the counts per second of the Hf 4f_{7/2} spectra at 0.6 nm for different plasma powers (the inset).

Once an oxygen dumbbell pair formed between two cations, the electron donation from the second nearest-neighboring Hf atoms is decreased, causing the electron density on the metal atom slightly decreases. In this case, the screening effect of the metal core-levels reduces, and thereby, increasing the measured BE.²⁵

The formation of O-O covalent bonds leads to less negative net charges at O atoms, which are typically implied on a higher BE in the corresponding O 1s photoelectrons.²⁶ This is in agreement with the O 1s spectra that broaden to the higher energy, as shown in Figure 7(b) and (d). The exchange in the peak predominance of O_I to O_{II} at the surface reveals that the oxidized lattice oxygen loses some negative charges as oxygen further injected after the stoichiometry is formed. In this case, the excess oxygen may capture the charges to form the aforementioned covalent bonding. Thus, in O-rich condition, the O_{II} peak corresponds to the nonstoichiometry in the presence of O-O bonds. On the other hand, the emergence of a small shoulder at a higher BE (O_{III}) is typically attributed to the loosely bound hydroxyl groups, such as adsorbed -OH or O₂.^{34,38,40,46} In S200 and S300, the surface hydroxylation might be permeated, because the greater concentration of oxygen on the HfO_x surface can strongly attract the water molecules from the ambient, as confirmed by the contact angle analysis in Figure 2(b).

The different tendencies observed in S200 and S300 suggest that the Hf-O bond formed during the plasma treatment differs from that formed in the annealing process. The oxygen bonds generated by the plasma treatment may appear through an enforcement process. In the absence of high-temperature annealing, the defects must be frozen and correspondingly produce a greater energy barrier hindering oxygen from incorporating into the vacant sites.¹⁴ Thus, the incoming oxygen ions must gain sufficient energy to breach the barrier energy before filling up the nearby vacancies around the Hf atoms.^{20,33}

The source for such high energy strength may come from the electron discharge power during the plasma generation that induces sheath potential to accelerate oxygen ions toward the sample.⁴⁷ This process provides bombardment energy for the oxygen ions to diffuse and bind with the Hf atoms. In S100, the 100 W RF power applied provides an ion energy that is sufficiently high to breach the a-HfO_x barrier around the surface, allowing the incoming oxygen to fill the vacancies and form stoichiometric layers close to the interface (0.6 nm). As illustrated in Figure 5(a), the Hf-O bonds previously relaxed by the presence of the V_O²⁺ are restored upon the oxygen incorporation. This process causes a lowering in the Hf 4f main peaks and reduction in the Hf²⁺-O and Hf⁰-metal peaks, as shown in Figure 6(a). Such a bombardment mechanism may be the reason why the amorphousness of the film is preserved even after the stoichiometry is formed. In the samples with higher power (S200 and S300), both the plasma density and ion energy are probably increased.^{14,47} This situation allows more oxygen to penetrate and occasionally induces bombardment damage to the film surface. Once a more energetic oxygen ion impinges on the film, the stoichiometry of the deeper level can be constructed. This process is accompanied by a greater lattice relaxation along the propagation path that may break the previously formed stoichiometric Hf-O bonds.⁴⁸ These breaking are expressed in the reduction of the Hf 4f signal counts on the surface layers with respect to the power increases, as shown in the inset of Figure 8. The relaxation induces a larger potential barrier that makes it more difficult for the next incoming oxygen atom to bind with neighboring Hf atoms,¹⁴ although the oxygen atoms are continually provided by the high plasma density. Alternatively, the excess oxygen ions may present as atomic interstitials, and subsequently establish their present by bonding to lattice O via O-O covalent bonds, as elaborated previously.

To this point, it has been demonstrated that different oxygen plasma powers can induce different oxygen states in the HfO_x film. We now have four different chemical conditions of the HfO_x samples: a non-treated sample (S0), a sample with a stoichiometric surface (S100), a sample with a deeper stoichiometric layer but a few nonstoichiometric layers at the surface (S200), and a sample with more stoichiometric layers but also more nonstoichiometric layers at the surface (S300). Investigation on the effect of these different chemistries on the electrical performance yields interesting results. For simplicity, we tested these dielectrics using MIM capacitors and then choose the sample with the optimal conditions (*i.e.* better uniformity, lower leakage current and higher breakdown field) to fabricate an amorphous IGZO-based TFT.

The MIM capacitors examined in this paper have the same structure as the HfO_x investigated in the preceding paragraphs, only with the addition of Al as the top electrode, as drawn in Figure 9(a). In the use of high- κ oxide as the insulator layer, the benchmark point to characterize its performance is based on the nonlinear coefficient (α) of the quadratic voltage-capacitance ($\frac{\Delta C}{C_0} \propto \alpha V^2$).² This characterization is important because the

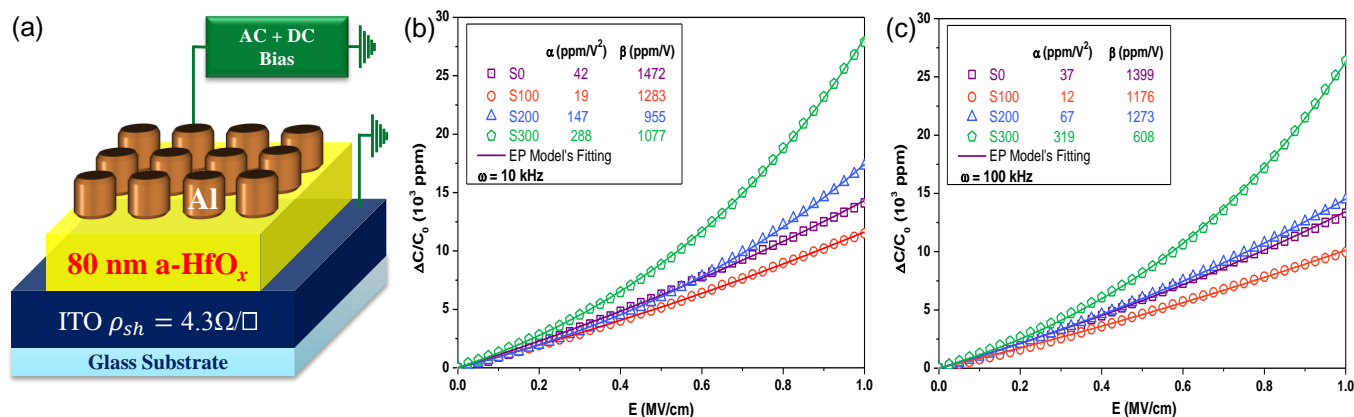


Figure 9. (a) Schematic structure of the MIM capacitors. Normalized capacitance vs. electric field characteristics of HfO_x MIM capacitors with various plasma treatment powers, for (b) low frequency (10 kHz) and (c) high frequency (100 kHz).

magnitude of α is strongly dependent on the dielectric constant⁴⁹ and must be preserved under 100 ppm/V² to maintain the device precision.² Fortunately, as depicted in Figure 9(b) and (c), the obtained α values are lower than 50 ppm/V² in the barely deposited a-HfO_x capacitor (S0) and decrease upon introducing the 100 W plasma treatments, which exhibits the lowest α at both low (19 ppm/V²) and high frequencies (12 ppm/V²). Improvements in the dispersion of the capacitance frequency dependency are also shown in Figure 10. These should have a correlation with the stoichiometry on the surface of this sample, as confirmed by XPS. Because when excess oxygen was induced at the surface (as in S200 and S300), the α value and the frequency dispersion are elevated, regardless of how deep the stoichiometric layers are formed. To understand the responsible chemistry, the underlying physical mechanism behind such nonlinearity must be understood.

The phenomenon has recently been explained by the electrode polarization model proposed by Gonon *et al.*^{17,50–53} This model was derived based on a dielectric relaxation mechanism in which the mobile ions in the bulk drift toward the electrode as a result of the electric field and accumulated in the interface over a Debye length (L_D).⁵⁰ The induced charges of the accumulated ions lead to the voltage and frequency dependency of the double-layer capacitance, revealing the nonlinear behavior of the capacitance.^{52–54} Accordingly, the capacitance density is increased by either increasing the DC field or decreasing the frequency as follows:⁵⁰

$$\frac{\Delta C}{C_0} = \frac{2}{(\epsilon_0 \epsilon)^{2n}} \left(\frac{L}{L_D}\right)^{1-2n} \frac{1}{(\rho+2)^{2(1-n)}} \frac{\sigma_0^{2n}}{\omega^{2n}} e^{\frac{nqEs}{kT}}, \quad (1)$$

$$\frac{\Delta C}{C_0} = A \left(\frac{\omega_c}{\omega}\right)^{-2n} \quad \text{where } 0 < 2n < 1, \quad (2)$$

where $A = \frac{2L}{(2+\rho)^2 L_D}$, $\omega_c = \frac{\sigma}{2\pi\epsilon_0\epsilon} \sqrt{\frac{2L_D}{L}}$, $L_D = \sqrt{\frac{\epsilon_0\epsilon k_B T}{Ne^2}}$, n is the Jonscher response, L is the film thickness, ϵ is the bulk dielectric permittivity, s is the hopping distance, N is the density of accumulated charges ($N \approx \frac{1}{s^3}$) and ρ is the electrode blocking parameter that determines the transparency of charge transfer at the electrode ($\rho = 0$ for blocking contact and $\rho = \infty$ for Ohmic contact). In the equations, the blocking parameter ρ is the only parameter adjusted to fit the experimental data, whereas the others are obtained directly from the fittings. For instance, the values of $2n$ were extracted from the logarithmic slope of the normalized capacitance-frequency curves presented in the inset of Figure 10(a) and (b). By fixing $2n$ at a certain frequency, s can be determined by taking the exponential fitting of the C-E curves in Figure 9. Additionally, from the known fitting parameters, the effective barrier (ϕ_i) for the AC charge transfer at the metal-oxide interface can be calculated from $\rho = \frac{avL}{D} \exp\left(-\frac{\phi_i}{kT}\right)$.^{50,55} Thus, a qualitative description of the effect of stoichiometry on the capacitor performance can be examined by fitting the equations to the capacitance dependences of both the voltage and frequency results in Figure 9 and Figure 10. As shown in the figures, our data trend and fittings are in an excellent agreement with the model.

The parameters extracted from the fittings are presented in Table 1. The calculated barrier ϕ_i in the treated samples is improved relative to the non-treated one (0.66 eV), particularly in S100 (0.80 eV) and S200 (0.82 eV). These larger barriers are attributed to the formation of the stoichiometric layer by the plasma treatment. This layer provides an optimum ratio of Hf and O atoms to avoid point defects that can act as a path for charge migration, forming the aforementioned double-layer

Table 1. Parameters describing the capacitance-voltage dependency of MIM capacitors with respect to the O₂ plasma power variations

Parameters	$\omega = 10$ kHz				$\omega = 100$ kHz			
	S0	S100	S200	S300	S0	S100	S200	S300
s (nm)	5.6	17.7	11.9	23.7	5.9	15.3	6.8	2.5
N (cm ⁻³)	5.5×10^{18}	1.8×10^{17}	6.0×10^{17}	7.5×10^{19}	4.9×10^{18}	2.8×10^{17}	3.2×10^{18}	6.6×10^{19}
σ_0 (S/cm)	1.69×10^{-8}	9.57×10^{-11}	5.18×10^{-11}	5.14×10^{-11}	1.69×10^{-8}	9.57×10^{-11}	5.18×10^{-11}	5.14×10^{-11}
ρ	69.1	19.1	18.1	1.02×10^{12}	41.7	18.4	7.5	1.06×10^{16}
L_D (nm)	2.02	11.2	6.2	0.55	2.2	9.0	2.7	0.6
ϕ_i (eV)	0.66	0.80	0.82	0.28	0.67	0.80	0.87	0.04

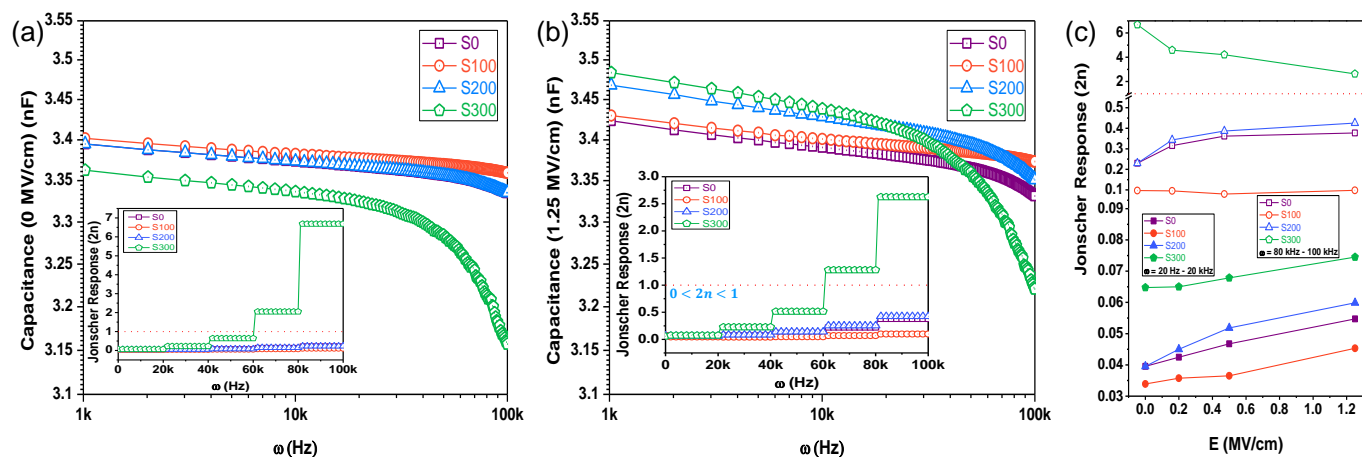


Figure 10. (a) Capacitance vs. frequency characteristics of the HfO_x capacitors in constant DC fields of (a) 0 MV/cm and (b) 1.25 MV/cm. (c) Electric field dependence of the Jonscher frequency response in low frequency (< 20 kHz) and high frequency regimes (> 80 kHz).

capacitances on the interfaces. This can be seen from the reduction of the accumulated charge density (N) of S100 in Table 1 ($5.5 \times 10^{18} \rightarrow 1.8 \times 10^{17} \text{ cm}^{-3}$) and explains the voltage nonlinearity improvement observed in Figure 9 ($\alpha = 37 \rightarrow 12 \text{ ppm/V}^2$). However, Table 1 indicates that N is increased in the higher-power samples of S200 and S300. This larger defect density is attributed to the O-rich states that occur on the surface, as elucidated by XPS. These stoichiometric imperfections can act as interface charge trappers, restoring the nonlinearity behavior in the capacitors.⁵¹ Hence, they might be responsible for the elevation of α to 147 ppm/V² and 288 ppm/V² in S200 and S300, respectively. This indicates that the voltage nonlinearity is more sensitive to the interface condition than to the bulk properties, which is in accordance with previously reported works.^{13,52,53}

Figure 10 shows the frequency dependency of the capacitance of the capacitors. At frequencies below 10 kHz, the space charges induced by the movement of the oxygen vacancies will have more time to be modulated by the AC signal, and hence a higher capacitance will be obtained.^{50,56} However, since all depositions and measurements were conducted at room temperature (21 °C), nearly flat capacitances were recorded in the low frequency regime. It appears that the dispersions are lower than 0.1 nF, even when a high DC field is applied, because the long-range ionic displacement requires thermal activation energy to shift the cut-off frequency (ω_c) toward the higher frequency, constructing the conduction path of the ions as the electric field is applied.^{17,53,57} At room

temperature, ω_c is below 10 Hz, so the electrode polarization effect prefers to be electronic, *i.e.*, the electrons hop via the vacancies rather than the ions themselves moving.^{50,53} This is in agreement with the calculated hopping distance shown in Table 1, which is two orders of magnitude higher than the interatomic distance. In addition, the slight increases in the capacitances and frequency responses ($2n$) produced in Figure 10(b) and (c) verify such electronic hopping conduction. As DC fields up to 1.25 MV/cm are applied, more electrons are injected into the electrode, driving more charges to migrate via the oxygen vacancies towards the opposite electrode. In that case, the double-layer capacitance will be upgraded, leading to a slightly higher capacitance and frequency dispersion.⁵³

By increasing the frequency, the polarization effect is weakened and the capacitance is reduced, obeying the Jonscher power law, as stated in Eq. 2.⁵⁸ As shown in Figure 10, the slope of the dispersions for S0, S100 and S200 capacitors are found to follow this power law ($2n < 1$). However, stronger frequency dependence is observed in S300. Above 60 kHz, the slope increases drastically, exceeding the power law.⁵⁶ Das *et al.* reported a similar dispersion in Pr_{0.7}Ca_{0.3}MnO₃ oxide, which was ascribed to carrier relaxation in deep traps.⁵⁹ For HfO₂ MIMs, Gonon *et al.* recently reported that the abrupt decrease in frequency is due to a series resistance from the sputtered top electrode.⁶⁰ The additional vacancies produced by different electrode oxygen-affinity shift ω_c over 1 kHz. However, in this work, we used the same top electrode condition for all capacitors, but only S300 showed this large dispersion. Therefore, the large oxygen defects (probably O-O bonds) on the interface may be responsible for significantly larger charge densities, because these defects can act as deep-traps in Hafnia.^{14,20} At such a large defect density, L_D becomes

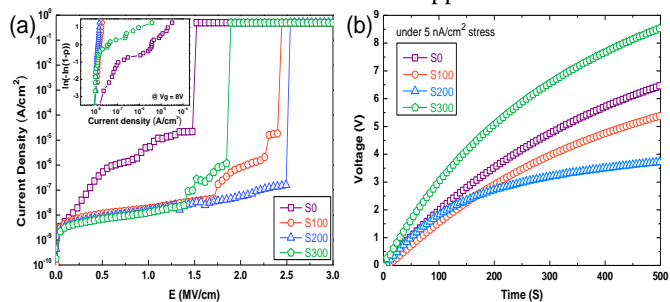


Figure 11. (a) Leakage current, breakdown voltage, leakage current uniformity (the inset) and (b) constant-current stress variation by the plasma treatment.

Table 2. Parameters extracted from the leakage current and constant stress measurements.

Parameters	S0	S100	S200	S300
Leakage current density (nA/cm ²) at $E = 1 \text{ MV/cm}$	5,300	19	15	13
Breakdown field (MV/cm)	1.47	2.40	2.49	1.85
CCS voltage shift (V)	6.46	5.38	3.72	8.53

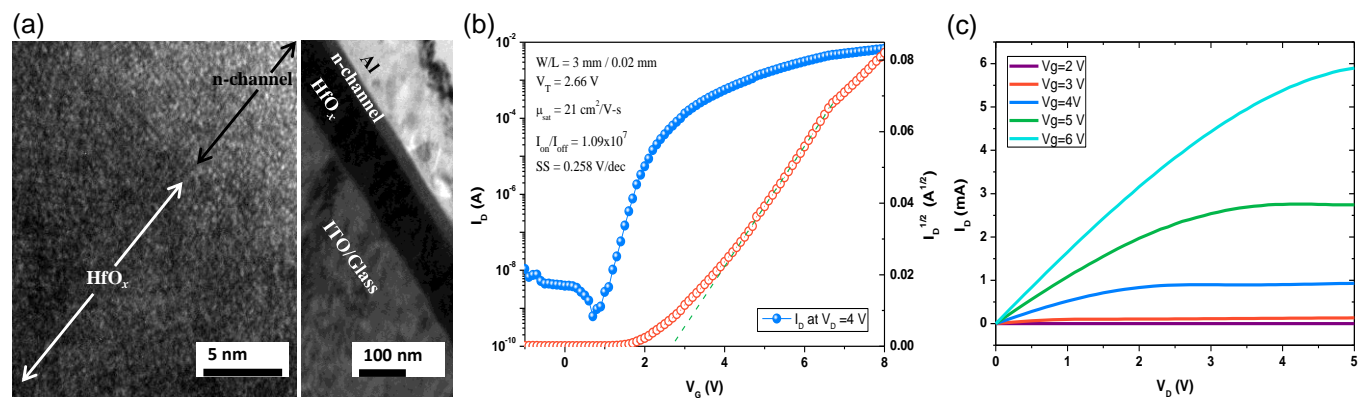


Figure 12. Implementation of the S200 HfO_x as a bottom-gate dielectric insulator in an IGZO-TFT.

extremely thin, allowing electrons to tunnel from the metal cathode to the defect traps within the dielectric.⁶¹ One can also see that the AC barrier is diminished to 0.04 eV in this sample due to the high value of the blocking electrode coefficient ($\rho = 9.7 \times 10^{15}$), which is a consequence of the large frequency dispersion ($2n = 2.6$). This parameter reflects a poor blocking contact at the S300 interface, giving rise to the massive electron injection from the electrode into the defect sites.^{50,55} This electron leakage causes a strong capacitance nonlinearity in both voltage and frequency, as observed in Figure 9 and Figure 10.

To confirm the implementation of the HfO_x films as a gate oxide in TFT, we sputtered an n-type channel a-IGZO on the top of the preceding HfO_x/ITO structure and then deposited Al as its S/D contact. As indicated in the TEM images in Figure 12(a), the amorphousness of both the sputtered gate oxide and n-channel are preserved. Thus, an amorphous n-TFT has been fabricated. For brevity, we demonstrate only the optimal sample in this paper. In contrast with the MIM, for the TFT device, S200 is found to be preferable to S100. The thicker stoichiometry in S200 promotes a higher breakdown field of 2.49 MV/cm and a lower leakage current of 1.2×10^{-8} A/cm² at 1 MV/cm, as indicated in Figure 11(a). Table 2 shows that these results are improved over those of S100. Moreover, the thicker stoichiometry can overcome the greater surface roughness on the film, giving a better device uniformity, as shown in the Weibull distributions of the leakage current in the inset of Figure 11(a).¹⁹ Furthermore, the presence of a small amount of residual oxygen is preferable here, as they could be easily captured by an oxygen deficiency domain on the channel-oxide interface during the IGZO deposition. Filling up the vacancies can reduce the scattering center so that a higher field-effect mobility of $21 \text{ cm}^2/\text{V}\cdot\text{s}$ is obtained here.⁶² This follows from the lower constant current stress (CCS) voltage shift of 3.72 V observed in Figure 11(b) for this sample. This means that S200 offers fewer charge trapping defects in the channel interface than the other samples. On the other hands, although S300 provides even thicker stoichiometric layers, the presence of an excessive amount of oxygen may cause more charge-trapping effects, resulting in an elevation of the CCS voltage shift followed by a decrease in the breakdown strength

and leakage uniformity. In TFT, this will degrade the threshold voltage (V_T), subthreshold swing (SS) and TFT mobility.^{3,63}

Finally, the transfer characteristics of the implementation of S200 in a-IGZO TFT are displayed in Figure 12(b) and (c). Surprisingly, even without employing any thermal annealing treatment, a small positive V_T of 2.66 V, a high $I_{\text{on}}/I_{\text{off}}$ ratio of 1.09×10^7 and a reasonable SS of 0.258 V/dec can be achieved. In fact, the characteristics are improved compared to the recently reported high-performance sputtered work.⁶⁴ Therefore, this outcome indicates the potential use of plasma treatment in the preparation of gate dielectrics for room-temperature TFTs.

Conclusions

The role of oxygen plasma treatment on the defect chemistries of the HfO_x dielectric films, including their effects on the electrical properties of MIM capacitors and TFTs, has been evaluated. XPS confirms the presence of various stoichiometries in the films after exposure to different powers of oxygen plasma treatment. The stoichiometry is characterized by a narrowing of the Hf $4f_{7/2}$ peak at 17.4 eV together with the fully enhancement of O_I peak. Otherwise, the spectra can be argued relating to the formation of oxygen defects, *i.e.*, oxygen vacancies for Hf-rich, and O-O bonds and hydroxyl groups for O-rich. In the devices implementation, the formation of a stoichiometric surface (S100) was found to be in line with the improvement of the quadratic voltage coefficient and frequency dispersion of the capacitances, and thickening the stoichiometric layer (S200) contributed to enhancement of the leakage current density, device uniformity and breakdown field strength. The first characteristic gives optimum performance for the MIM capacitors, whereas the latter favors TFT. However, despite the stoichiometry, applying this higher ion energy can cause erosion damage to the HfO_x film, leading to the appearance of residual oxygen on the top of the formed stoichiometric level. The presence of these defects aggravates the voltage nonlinearity, frequency dispersion, breakdown field and device uniformity (S300). Nevertheless, this observation confirms the bombardment mechanism during the passivation that kept the sample amorphous. This is in contrast to the high-temperature process that generally induces the rapid growth of

crystallization and grain boundaries. It also verifies that the dielectric interface plays a greater role in device performance than the nature of the bulk. Therefore, this work provides insight for understanding and developing a room-temperature procedure for preparing HfO₂ dielectric oxide. The process can be extended to organic flexible substrates, which is currently under investigation.

Acknowledgements

This work was supported by Ministry of Science and Technology Taiwan, ROC (NSC-102-2325-B-182-006).

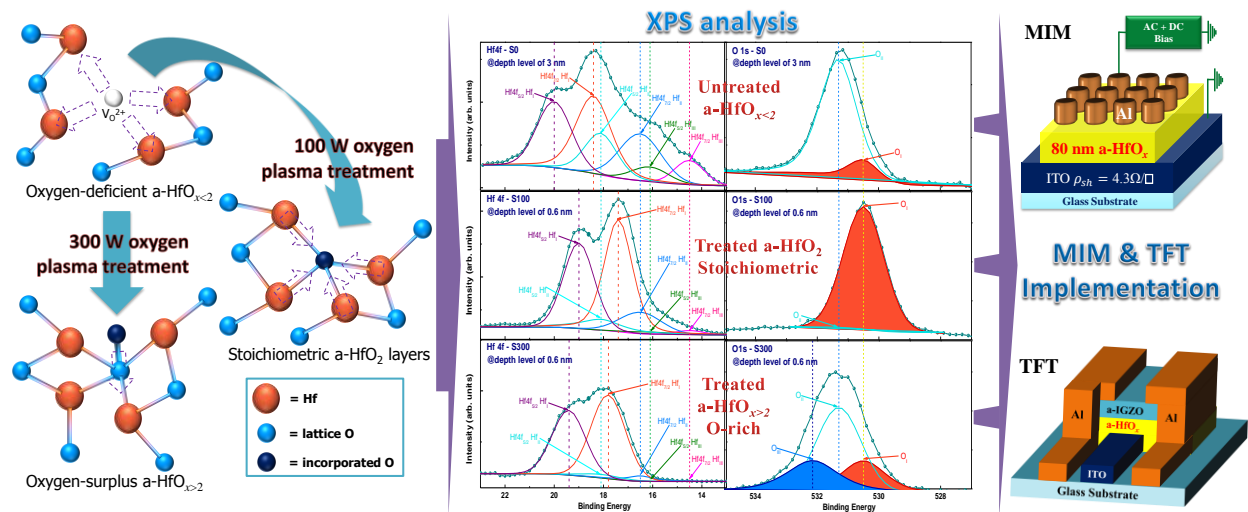
Notes and references

Department of Electronic Engineering, Chang Gung University, Tao-Yuan, 33302, Taiwan ROC

- L. Y. Liang, H. T. Cao, Q. Liu, K. M. Jiang, Z. M. Liu, F. Zhuge and F. L. Deng, *ACS Appl. Mater. Interfaces*, 2014, **6**, 2255–2261.
- ITRS, *ITRS: Radio Frequency and Analog/Mixed-Signal Technologies for Communications 2011 Report*, 2011.
- P. K. Nayak, M. N. Hedhili, D. Cha and H. N. Alshareef, *Appl. Phys. Lett.*, 2012, **100**, 202106.
- S. R. Forrest, *Nature*, 2004, **428**, 911–8.
- D. Tobjörk and R. Österbacka, *Adv. Mater.*, 2011, **23**, 1935–1961.
- S. W. Nam, J. H. Yoo, S. Nam, H. J. Choi, D. Lee, D. H. Ko, J. H. Moon, J. H. Ku and S. Choi, *J. Non. Cryst. Solids*, 2002, **303**, 139–143.
- G. He, L. Q. Zhu, M. Liu, Q. Fang and L. D. Zhang, *Appl. Surf. Sci.*, 2007, **253**, 3413–3418.
- J. H. Jang, H.-S. Jung, J. H. Kim, S. Y. Lee, C. S. Hwang and M. Kim, *J. Appl. Phys.*, 2011, **109**, 023718.
- G. He, M. Liu, L. Q. Zhu, M. Chang, Q. Fang and L. D. Zhang, *Surf. Sci.*, 2005, **576**, 67–75.
- S. C. Chen, T. C. Chang, H. H. Su, P. C. Yang, J. Lu, H. C. Huang, D. S. Gan, N. J. Ho and Y. Shi, *Mater. Lett.*, 2009, **63**, 1914–1916.
- H. S. Baik, M. Kim, G.-S. Park, S. A. Song, M. Varela, a. Franceschetti, S. T. Pantelides and S. J. Pennycook, *Appl. Phys. Lett.*, 2004, **85**, 672.
- D.-Y. Cho, H. S. Jung, I.-H. Yu, J. H. Yoon, H. K. Kim, S. Y. Lee, S. H. Jeon, S. Han, J. H. Kim, T. J. Park, B.-G. Park and C. S. Hwang, *Chem. Mater.*, 2012, **24**, 3534–3543.
- S. D. Park, C. Park, D. C. Gilmer, H. K. Park, C. Y. Kang, K. Y. Lim, C. Burham, J. Barnett, P. D. Kirsch, H. H. Tseng, R. Jammy and G. Y. Yeom, *Appl. Phys. Lett.*, 2009, **95**, 022905.
- A. S. Foster, A. L. Shluger and R. M. Nieminen, *Phys. Rev. Lett.*, 2002, **89**, 225901.
- K. McKenna and A. Shluger, *Appl. Phys. Lett.*, 2009, **95**, 222111.
- C. Y. Ma, W. J. Wang, J. Wang, C. Y. Miao, S. L. Li and Q. Y. Zhang, *Thin Solid Films*, 2013, **545**, 279–284.
- P. Gonon and F. El Kamel, *J. Appl. Phys.*, 2007, **101**, 073901.
- J. S. Meena, M.-C. Chu, S.-W. Kuo, F.-C. Chang and F.-H. Ko, *Phys. Chem. Chem. Phys.*, 2010, **12**, 2582–2589.
- K.-C. Liu, J.-R. Tsai, W.-K. Lin, C.-S. Li and J.-N. Chen, *Thin Solid Films*, 2011, **519**, 5110–5113.
- A. S. Foster, F. Lopez Gejo, A. L. Shluger and R. M. Nieminen, *Phys. Rev. B*, 2002, **65**, 174117.
- H. Y. Yu, X. D. Feng, D. Grozea, Z. H. Lu, R. N. S. Sodhi, A.-M. Hor and H. Aziz, *Appl. Phys. Lett.*, 2001, **78**, 2595.
- D. Raoufi, A. Kiasatpour, H. R. Fallah and A. S. H. Rozatian, *Appl. Surf. Sci.*, 2007, **253**, 9085–9090.
- K. Kukli, M. Ritala, T. Sajavaara, J. Keinonen and M. Leskelä, *Chem. Vap. Depos.*, 2002, **8**, 199–204.
- A. Salain, H. Grampeix, J. Buckley, C. Mannequin, C. Vallée, P. Gonon, S. Jeannot, C. Gaumer, M. Gros-Jean and V. Jousseume, *Thin Solid Films*, 2012, **525**, 20–27.
- R. L. Opila, G. D. Wilk, M. A. Alam, R. B. van Dover and B. W. Busch, *Appl. Phys. Lett.*, 2002, **81**, 1788.
- C. Driemeier, R. M. Wallace and I. J. R. Baumvol, *J. Appl. Phys.*, 2007, **102**, 024112.
- S. Suzer, S. Sayan, M. M. Banaszak Holl, E. Garfunkel, Z. Hussain and N. M. Hamdan, *J. Vac. Sci. Technol. A Vacuum, Surfaces, Film.*, 2003, **21**, 106.
- H. Y. Zhang, C. Ye, C. G. Jin, M. Z. Wu, Y. Y. Wang, Z. Zhang, T. Y. Huang, Y. Yang, H. J. He, L. J. Zhuge and X. M. Wu, *Appl. Surf. Sci.*, 2014, **311**, 117–123.
- J. F. Moulder, W. F. Stickle, P. E. Sobol and K. D. Bomben, *Handbook of X-ray Photoelectron Spectroscopy*, Perkin-Elmer Corporation, Physical Electronics Division: Eden Prairie, MN, 1992, vol. 3.
- S.-S. Lin and H.-R. Li, *Ceram. Int.*, 2013, **39**, 7677–7683.
- G. D. Wilk, R. M. Wallace and J. M. Anthony, *J. Appl. Phys.*, 2000, **87**, 484–492.
- M.-H. Cho, Y. S. Roh, C. N. Whang, K. Jeong, S. W. Nahm, D.-H. Ko, J. H. Lee, N. I. Lee and K. Fujihara, *Appl. Phys. Lett.*, 2002, **81**, 472.
- D. Y. Cho, C. H. Min, J. Kim, S. J. Oh and M. G. Kim, *Appl. Phys. Lett.*, 2006, **89**, 253510.
- C. Avis, Y. G. Kim and J. Jang, *J. Mater. Chem.*, 2012, **22**, 17415–17420.
- V. Cosnier, M. Olivier, G. Thérêt and B. André, *J. Vac. Sci. Technol. A Vacuum, Surfaces, Film.*, 2001, **19**, 2267.
- D.-Y. Cho, S. J. Oh, Y. J. Chang, T. W. Noh, R. Jung and J.-C. Lee, *Appl. Phys. Lett.*, 2006, **88**, 193502.
- N. Zhan, M. C. Poon, C. W. Kok, K. L. Ng and H. Wong, *J. Electrochem. Soc.*, 2003, **150**, F200–F202.
- J. S. Meena, M.-C. Chu, Y.-C. Chang, H.-C. You, R. Singh, P.-T. Liu, H.-P. D. Shieh, F.-C. Chang and F.-H. Ko, *J. Mater. Chem. C*, 2013, **1**, 6613.
- Y. Xue, H. He, Y. Jin, B. Lu, H. Cao, J. Jiang, S. Bai and Z. Ye, *Appl. Phys. A*, 2014, **114**, 509–513.
- M.-C. Chu, J. S. Meena, P.-T. Liu, H.-P. D. Shieh, H.-C. You, Y.-W. Tu, F.-C. Chang and F.-H. Ko, *Appl. Phys. Express*, 2013, **6**, 076501.
- N. Selvakumar, H. C. Barshilia, K. S. Rajam and A. Biswas, *Sol. Energy Mater. Sol. Cells*, 2010, **94**, 1412–1420.
- J. L. Gavartin, A. L. Shluger, A. S. Foster and G. I. Bersuker, *J. Appl. Phys.*, 2005, **97**, 053704.
- A. S. Foster, V. B. Sulimov, F. Lopez Gejo, A. L. Shluger and R. M. Nieminen, *Phys. Rev. B*, 2001, **64**, 224108.
- P. F. Lee, J. Y. Dai, K. H. Wong, H. L. W. Chan and C. L. Choy, *J. Appl. Phys.*, 2003, **93**, 3665.
- H. Y. Yu, M. F. Li, B. J. Cho, C. C. Yeo, M. S. Joo, D.-L. Kwong, J. S. Pan, C. H. Ang, J. Z. Zheng and S. Ramanathan, *Appl. Phys. Lett.*, 2002, **81**, 376.

- 46 D. Barreca, A. Milanov, R. A. Fischer, A. Devi and E. Tondello, *Surf. Sci. Spectra*, 2007, **14**, 34.
- 47 S. K. Ahn and H. Y. Chang, *Appl. Phys. Lett.*, 2009, **95**, 111502.
- 48 J. Chen, W. J. Yoo and D. S. H. Chan, *J. Vac. Sci. Technol. A Vacuum, Surfaces, Film.*, 2006, **24**, 133.
- 49 C. Wenger, G. Lupina, M. Lukosius, O. Seifarth, H.-J. Müssig, S. Pasko and C. Lohé, *J. Appl. Phys.*, 2008, **103**, 104103.
- 50 P. Gonon and C. Vallée, *Appl. Phys. Lett.*, 2007, **90**, 142906.
- 51 B. Miao, R. Mahapatra, R. Jenkins, J. Silvie, N. G. Wright and A. B. Horsfall, *Nucl. Sci. IEEE Trans.*, 2009, **56**, 2916–2924.
- 52 B. Miao, R. Mahapatra, N. Wright and A. B. Horsfall, *J. Appl. Phys.*, 2008, **104**, 054510.
- 53 F. El Kamel, P. Gonon and C. Vallée, *Appl. Phys. Lett.*, 2007, **91**, 172909.
- 54 C. Vallée, P. Gonon, C. Jorel and F. El Kamel, *Appl. Phys. Lett.*, 2010, **96**, 233504.
- 55 J. H. Beaumont and P. W. M. Jacobs, *J. Phys. Chem. Solids*, 1967, **28**, 657–667.
- 56 D. L. Sidebottom, *Phys. Rev. B*, 2000, **61**, 14507–14516.
- 57 O. Khaldi, F. Jomni, P. Gonon, C. Mannequin and B. Yangui, *Appl. Phys. A*, 2014, **116**, 1647–1653.
- 58 T. Bertaud, S. Blonkowski, C. Bermond, C. Vallee, P. Gonon, M. Gros-Jean and B. Flechet, *IEEE Electron Device Lett.*, 2010, **31**, 114–116.
- 59 N. Das, S. Tsui, Y. Y. Xue, Y. Q. Wang and C. W. Chu, *Phys. Rev. B*, 2008, **78**, 235418.
- 60 P. Gonon, M. Mougnot, C. Vallée, C. Jorel, V. Jousseume, H. Grampeix and F. El Kamel, *J. Appl. Phys.*, 2010, **107**, 074507.
- 61 F. El Kamel, P. Gonon, F. Jomni and B. Yangui, *Appl. Phys. Lett.*, 2008, **93**, 042904.
- 62 C.-J. Ku, Z. Duan, P. I. Reyes, Y. Lu, Y. Xu, C.-L. Hsueh and E. Garfunkel, *Appl. Phys. Lett.*, 2011, **98**, 123511.
- 63 K. Nomura, T. Kamiya, H. Ohta, M. Hirano and H. Hosono, *Appl. Phys. Lett.*, 2008, **93**, 192107.
- 64 J. S. Lee, S. Chang, S. M. Koo and S. Y. Lee, *IEEE Electron Device Lett.*, 2010, **31**, 225–227.

Table of contents entry



Oxygen plasma treatment controls different stoichiometry on the surface of a-HfO_x films, giving a recipe to fabricate MIM and TFT devices at room-temperature.